UNIVERSITY OF CALIFORNIA,
IRVINE

Simulation of DBD Plasma Flow Control with a High-Order Flow Solver

submitted in partial satisfaction of the requirements
for the degree of

MASTER OF SCIENCE

in Mechanical and Aerospace Engineering

by

Yifan Bai

Thesis Committee:
Professor Feng Liu, Chair
Professor Dimitri Papamoschou
Professor Haithem Taha

2018

TABLE OF CONTENTS

LIST OF FIGURES

LIST OF TABLES

NOMENCLATURE

In the Actuator Model

ε	Permittivity of the medium
ε_0	Permittivity of the free space
ε_r	Relative permittivity
$\vec{E}$	Electric field strength
$\vec{f_b}$	Body force
λ_d	Characteristic length for electrostatic shielding
Φ	Electric potential
ϕ	Electric potential produced by the charge density
φ	Electric potential related to the external field
ρ_c	Charge density

In the Flux Reconstruction Approach

$\square^{(f)}$	Variables defined on the flux points
$\square^{(u)}$	Variables defined on the solution points
$\tilde{\square}$	Veriables in the transformed space
$\tilde{f}_\alpha^{(f_\perp)}$	Flux in the direction of the surface normal
$\delta_{\rho\sigma}$	Kronecker delta
$\mathfrak{F}_\alpha$	Interface flux
$\mathbf{g}_{e\rho}^{(f)}$	Correction function associated with flux point ρ in element type e
$\mathbf{J}_{en}$	Transformation Jacobian for the n-th element of element type e
J_{en}	Determinant of the transformation Jacobian for the n-th element of element type e
$l_{e\rho}^{(u)}$	Nodal basis associated with the ρ-th solution point in element type e
$\mathcal{M}_{en}$	Mapping to the physical space for the n-th element of element type e
$\hat{\tilde{\mathbf{n}}}_{e\sigma}^{(f)}$	Unit normal at the σ-th flux point in element type e

Others

$\square^*$	Nondimensional variables
C_D	Drag coefficient
C_L	Lift coefficient
Re	Freestream Reynolds number

ACKNOWLEDGMENTS

I would like to express my gratefulness to my advisor Feng Liu. He has been a very helpful advisor. I started working in his group with only a little knowledge on numerical methods and programming. Professor Liu has been very patient and has given me enough time to explore. He even taught me my first lesson on Linux! I feel grateful for the effort he has put in helping me find my own interest and carry out a relatively independent research study.

I would also like to thank the other members on my thesis committee, professor Dimitri Papamoschou and professor Haithem Taha. Thanks for the time they have contributed. Professor Papamoschou has provided some detailed suggestions on the writing of this thesis.

Thanks to my parents for the financial support, which has made everything possible.

Thanks to my friends for keeping me company.

The work in this thesis was done almost entirely with open-source programs. Two open-source solvers, PyFR [4] and GetDP [5] were employed and introduced in this thesis. The unstructured meshes were generated in Gmsh [6], a light and handy open-source grid generator. The figures were all generated either in or with the help of the open-source post-processing software VisIt [7]. Thanks to the authors of these programs and those who has written the libraries they are based on. It is truly amazing how sharing and collaborations are creating an amiable environment for research.

ABSTRACT OF THE THESIS

Simulation of DBD Plasma Flow Control
with a High-Order Flow Solver

By

Yifan Bai

Master of Science in Mechanical and Aerospace Engineering

University of California, Irvine, 2018

Professor Feng Liu, Chair

A numerical simulation was performed for a 2D plasma flow control of flow around a circular cylinder at Reynolds number 6.6×10^3. The plasma actuator model proposed by Suzen *et al.* [1] was used. Poisson equations for the electric potential and the charge density were solved to compute the body force field. The body force generated by the plasma actuator model was incorporated into the flow solver as source terms for the momentum equations. The simulation with plasma actuators demonstrated a smaller wake and reduced vortex shedding behind the cylinder compared to the reference case without the actuators. The influence of the locations of the plasma actuators was investigated with a parametric study. The results indicate that the effectiveness of the plasma actuation is sensitive to the actuator locations.

Chapter 1

Introduction to the DBD Plasma Actuator

1.1 Configuration and Mechanism

The dielectric barrier discharge (DBD) plasma actuators for flow control have been extensively studied in the past 20 years. They have been attractive among ways of active flow control for their fast response, small weight, negligible impact on the shape of the mounted surface and high power efficiency [8]. The configuration for a single dielectric barrier discharge (SDBD) actuator is shown in Fig. 1.1. It consists of two electrodes, separated by a dielectric barrier. One of the electrodes is exposed in air, the other is embedded in the dielectric material.

When a sufficiently high voltage is applied to the electrodes, the air in the vicinity of the electrodes will be lightly ionized and create the plasma. The plasma is composed of charged components yet net neutral, containing as many negative electrons as positive ions. It spreads out from the edge of the exposed electrode to the side above

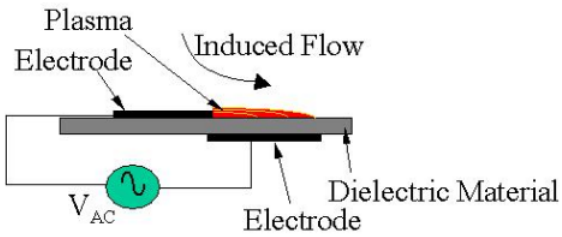

Figure 1.1: Configuration of the DBD plasma actuator [1].

the embedded electrode.

The plasma actuators usually operate with a high AC voltage supplied, typically 5-20kV with a frequency range from 3 to 15 kHz. With the external electric field, the electrons move to the positive electrode and the ions to the negative electrode. Momentum is transferred from the plasma discharge to the ambient air through collisions of ions, which cause a body force vector acting on the external flow, sometimes referred to as the electrohydrodynamic (EDH) force [9].

The body force entrains and accelerates the surrounding air. When initiated in quiescent air the body force generally induces a spanwise starting vortex, moving along and away from the wall, which later on leads to the formulation of a jet tangential to the actuator wall that alters the flow field over the actuator surface [3]. This has been observed in both experiments and numerical simulations of initiation of plasma actuators in quiescent air and will be discussed with greater details when presented as the results of this study in chapter 4.

1.2 Applications to bluff body flow control

The flow around a bluff body demonstrates complex fluid dynamics phenomena, including the transition of the boundary layer, flow separation and the formulation of

the wake behind the body. Therefore it offers excellent settings to study flow control techniques.

The plasma actuators have been successfully applied to different flow control situations. A partial list of examples includes separation control over a conical fore-body [10, 11, 12, 13, 14], a circular cylinder [2, 15], a high angle of attack airfoil [16] and turbine blades [17]. They have been proven to be effective for drag reduction [18], and lift improvement [19].

The flow around a circular cylinder is a classic scenario that has been extensively studied over a wide range of Reynolds numbers. It has been well documented [20] and is therefore often used as a canonical case for studying plasma actuators, both experimentally [2, 15, 21] and numerically [22, 23, 24].

There are many factors that affect the performance of the plasma actuators when they are applied to flow control, including the locations of the actuators on the surface, orientation, size and relative placement of the embedded and exposed electrodes [1].

The actuators in the separation control experiments are usually installed close to the separation point. It is believed that the Coanda effect of the body force induced tangential jet plays a significant role in maintaining the flow attachment and delaying the separation [2].

The actuation can either be steady or unsteady. Fig. 1.2 illustrates the steady and unsteady input signals for the plasma actuators. As shown in the figure, the unsteady actuation needs to be performed with a certain frequency and duty cycle, and can either be symmetric or asymmetric when mounted in pairs onto a bluff body. Several experimental studies, including those performed by McLaughlin *et al.* [15] and Jukes and Choi [25] were able to show that pulsed forcing was more effective than continuous flow control.

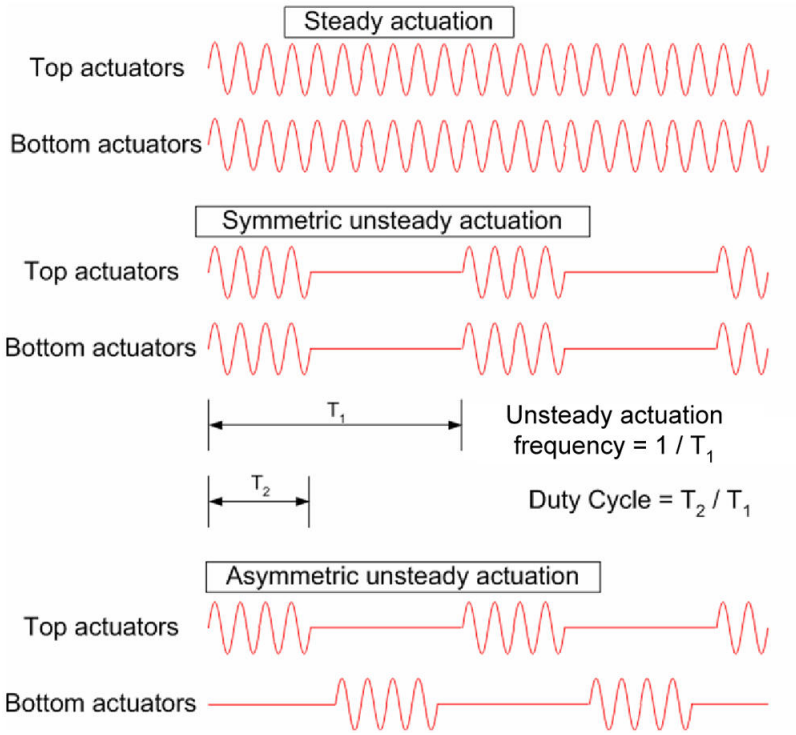

Figure 1.2: Steady and unsteady actuation signals [2].

The frequency and duty cycle when using unsteady actuation [2] can also affect the effectiveness of the actuators. Thomas *et al.* [2] have shown via experimental results that an unsteady frequency close to the natural shedding frequency generates large amplitude Karman vortex shedding, whereas an actuation frequency of $St_D = fD/U_\infty = 1$ produces an optimal flow control efficiency. Here, f is the frequency of the unsteady signal, D is the diameter of the cylinder and U_∞ is the incoming flow velocity. On the other hand, they have found in the same study that lowering the duty cycle does not largely compromise the effectiveness as long as the duty cycle is larger than 10%. Therefore it is possible to reduce the power consumption by decreasing the duty cycle to a reasonable value.

1.3 Objectives

The studies of the plasma actuator focus on either understanding the physics of the DBD, or optimizing the plasma actuator to improve its performance. The purpose of this study is the latter one.

The effect of the factors that influence the plasma actuator performance can be studied relatively cheaper with numerical simulations since adjusting the parameters in computations costs less than in experiments. Large eddy simulations were carried out by Kim and Wang [24] and Rizetta and Visbal [23] for plasma flow control of flow around a circular cylinder. The effect of the unsteady frequency was studied in the case of Kim and Wang while the influence of the symmetric and asymmetric actuation was investigated by Rizetta and Visbal.

Although the plasma flow control was heavily studied via experiments, the amount of numerical studies of this application is still limited. The work in this thesis implemented a high order flow solver to the study of plasma flow control. The results can be viewed as a validation of the experiments. Meanwhile the parametric study of the key factors can be used to improve the plasma actuator performance. Additionally, the high order solver gives a better resolution of the flow field, which will become a more significant advantage when extending the study to three dimension.

There are various models for the plasma actuators. Suzen *et al.* proposed a simple model in 2007, which solves the electric potential equations [1]. This model is basically a variation of the classic electrostatic model. By decomposing the electric potential, their model was able to produce a body force vector field with a correct general orientation. Orlov and colleagues developed the lumped-element model, which models the plasma, surrounding air and the dielectric barrier with lumped circuit elements [26]. The results of the lumped-circuit model served as boundary conditions for the

electric potential equation. Their model eliminates the incorrect body force scaling of V_{AC}^2 which presents in the electrostatic model, and produces a correct scaling of $V_{AC}^{7/2}$. An example of a more complex model is the three-element module proposed by Boeuf *et al.*, which involves solving the transportation equations of the electrons, positive and negative ions [27].

Despite the complex physics of the DBD and the existing more sophisticated modules which capture the behaviour of the plasma actuators more accurately, the simple model proposed by Suzen *et al.* was adopted for this study. Since the goal is to study the factors affecting the actuator performance, using a simpler model that provides qualitatively correct simulations does not diminish the purpose, and is more economic.

Chapter 2

Numerical Methods

2.1 Flow Solver: PyFR

The high-order flow solver used in this study is PyFR, an open source Navier-Stokes solver based on the flux reconstruction (FR) approach [4]. A brief introduction to the FR schemes and the solver is given in this chapter.

2.1.1 The Flux Reconstruction Approach

The FR approach was first introduced in 2007 by Huynh [28]. Huynh demonstrated in his paper that several high-order schemes, including the discontinuous Galerkin (DG) and the spectral difference (SD) schemes can be derived within the single unified FR framework.

Later on, with the work done by Vincent *et al.* [29] to identify a group of energy stable FR schemes, the FR approach is able to serve as a way of constructing new high-order schemes with improved properties. Huynh's paper demonstrated the construction of

the FR schemes for 1D linear convective equation. A large amount of work has been done in recent years to extend the FR approach to solving the Navier-stokes equations, i.e., nonlinear convection-diffusion equations on various types of elements in 2D and 3D [30, 31, 32], making it applicable to numerical simulations over complex geometries.

A significant advantage of the FR approach is that it is based on the differential form of the governing equations, which eliminates the trouble to perform surface integrals, making the FR schemes computationally cheaper and easier to implement [33].

A brief overview to the construction of the FR schemes for the Euler equations is given below following the notations from the introduction paper to PyFR [4]. Consider the convection equations:

$$\frac{\partial u_\alpha}{\partial t} + \nabla \cdot \mathbf{f}_\alpha \left(\mathbf{u} \right) = 0, \tag{2.1}$$

where $\mathbf{u}$ is the conservative variables and $\mathbf{f}_\alpha$ is the flux.

Inside the nth element of element type denoted by e, $\mathbf{\Omega}_{en}$,

$$\frac{\partial u_{en\alpha}}{\partial t} + \nabla \cdot \mathbf{f}_{en\alpha} = 0. \tag{2.2}$$

For implementation purpose the equations are first mapped to a standard element $\hat{\mathbf{\Omega}}_e$ in the transformed space $\tilde{\mathbf{x}}$. Taking the transformed solution and flux to be

$$\tilde{u}_{en\alpha}(\tilde{\mathbf{x}}, t) = J_{en}(\tilde{\mathbf{x}}) u_{en\alpha} \left(\mathcal{M}_{en}(\tilde{\mathbf{x}}), t \right), \tag{2.3a}$$

$$\tilde{\mathbf{f}}_{en\alpha}(\tilde{\mathbf{x}}, t) = J_{en}(\tilde{\mathbf{x}}) \mathbf{J}_{en}^{-1}(\tilde{\mathbf{x}}) \mathbf{f}_{en\alpha} \left(\mathcal{M}_{en}(\tilde{\mathbf{x}}), t \right), \tag{2.3b}$$

where $\mathcal{M}_{en}$ is the mapping, $\mathbf{J}_{en}$ is the transformation Jacobian and J_{en} is its determinant,

The transformed equations become

$$\frac{\partial u_{en\alpha}}{\partial t} + J_{en}^{-1}\tilde{\nabla}\cdot\tilde{\mathbf{f}}_{en\alpha} = 0. \tag{2.4}$$

Inside each element a set of solution points is defined. The first step of the FR approach is to construct a polynomial approximation for the conservative variables and the flux inside each element:

$$u_{en\alpha}^{(u)}(\tilde{\mathbf{x}}) = u_{e\rho n\alpha}^{(u)} l_{e\rho}^{(u)}(\tilde{\mathbf{x}}), \tag{2.5a}$$

$$\tilde{\mathbf{f}}_{en\alpha}^{(u)}(\tilde{\mathbf{x}}) = \tilde{\mathbf{f}}_{e\rho n\alpha}^{(u)} l_{e\rho}^{(u)}(\tilde{\mathbf{x}}), \tag{2.5b}$$

where superscript (u) denotes variables defined on the solution points, $l_{e\rho}^{(u)}(\tilde{\mathbf{x}})$ is the nodal basis associated with the ρ-th solution point in element type e. The transformations performed from arbitrary elements to standard elements allow the definition of one set of nodal basis for each element type. The element-wise constructed solution and flux are both discontinuous at each element interface.

Besides the solution points, a set of flux points is defined for each element at the interfaces, as shown in Fig. 2.1. Notice that the flux points at each interface are co-located for the two adjacent elements. The discontinuous solution and discontinuous flux are interpolated from the solution points to the flux points as:

$$u_{e\sigma n\alpha}^{(f)} = u_{e\rho n\alpha}^{(u)} l_{e\rho}^{(u)}(\tilde{\mathbf{x}}_{e\sigma}), \tag{2.6}$$

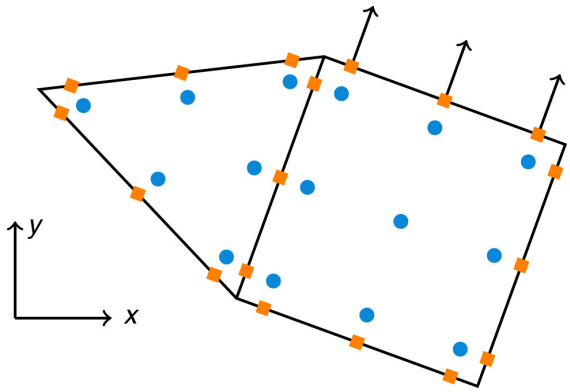

Figure 2.1: The solution points ● and flux points ■ on triangle and rectangle elements for $p = 2$. [4]

and

$$\tilde{f}^{(f_\perp)}_{e\sigma n\alpha} = l^{(u)}_{e\rho}(\tilde{\mathbf{x}}_{e\sigma})\hat{\tilde{\mathbf{n}}}^{(f)}_{e\sigma} \cdot \tilde{\mathbf{f}}^{(u)}_{e\rho n\alpha}, \tag{2.7}$$

where $\hat{\tilde{\mathbf{n}}}^{(f)}_{e\sigma}$ is the unit normal vector at the σ-th flux point in element type e.

A continuously defined flux is needed to form a continuous solution as indicated in Eq. 2.1. In order to "correct" the discontinuous flux, a common interface flux $\mathfrak{F}_\alpha$ can be defined as a function of the discontinuous solution and discontinuous flux constructed at the flux point for the two adjacent elements at each co-located flux point. The exact form of the interface flux depends on the nature of the governing equations. For convective equations an approximate Reimann solver, e.g. the Roe type solver [34], is mostly used to compute the upwinding flux.

A vector correction function $\mathbf{g}^{(f)}_{e\rho}(\tilde{\mathbf{x}})$ with property

$$\hat{\tilde{\mathbf{n}}}^{(f)}_{e\sigma} \cdot \mathbf{g}^{(f)}_{e\rho}\left(\tilde{\mathbf{x}}_{e\sigma}\right) = \delta_{\rho\sigma} \tag{2.8}$$

is associated with each flux point. Here, $\delta_{\rho\sigma}$ is the Kronecker delta. With this

correction function field the discontinuous flux inside each element is "corrected":

$$\begin{aligned}\tilde{\mathbf{f}}_{en\alpha}(\tilde{\mathbf{x}}) &= \mathbf{g}^{(f)}_{e\sigma}(\tilde{\mathbf{x}})\left[\mathfrak{F}_\alpha \tilde{f}^{(f_\perp)}_{e\sigma n\alpha} - \tilde{f}^{(f_\perp)}_{e\sigma n\alpha}\right] + \tilde{\mathbf{f}}^{(u)}_{en\alpha}(\tilde{\mathbf{x}}) \\ &= \mathbf{g}^{(f)}_{e\sigma}(\tilde{\mathbf{x}})\left[\mathfrak{F}_\alpha \tilde{f}^{(f_\perp)}_{e\sigma n\alpha} - \tilde{f}^{(f_\perp)}_{e\sigma n\alpha}\right] + \tilde{\mathbf{f}}^{(u)}_{e\nu n\alpha} l^{(u)}_{e\nu}(\tilde{\mathbf{x}}),\end{aligned} \tag{2.9}$$

where $\mathfrak{F}_\alpha \tilde{f}^{(f_\perp)}_{e\sigma n\alpha}$ is the interface flux at the σ-th flux point, $\left[\mathfrak{F}_\alpha \tilde{f}^{(f_\perp)}_{e\sigma n\alpha} - \tilde{f}^{(f_\perp)}_{e\sigma n\alpha}\right]$ is the "gap" between the interface flux and discontinuous flux. The continuous flux is "reconstructed" to match the interface flux on each element interface with the correction. Finally, the solution is advanced with the continuous flux:

$$\frac{\partial u^{(u)}_{e\rho n\alpha}}{\partial t} = -J^{-1(u)}_{e\rho n}(\tilde{\nabla}\cdot\tilde{\mathbf{f}})^{(u)}_{e\rho n\alpha}, \tag{2.10}$$

where

$$(\tilde{\nabla}\cdot\tilde{\mathbf{f}})^{(u)}_{e\rho n\alpha} = \left[\tilde{\nabla}\cdot\mathbf{g}^{(f)}_{e\sigma}(\tilde{\mathbf{x}})\left\{\mathfrak{F}_\alpha \tilde{f}^{(f_\perp)}_{e\sigma n\alpha} - \tilde{f}^{(f_\perp)}_{e\sigma n\alpha}\right\} + \tilde{\mathbf{f}}^{(u)}_{e\nu n\alpha}\cdot\tilde{\nabla} l^{(u)}_{e\nu}(\tilde{\mathbf{x}})\right]_{\tilde{\mathbf{x}}^{(u)}_{e\rho}}. \tag{2.11}$$

The flexibility of the FR schemes comes from the variation of choices for the correction function $\mathbf{g}^{(f)}_{e\rho}$. The DG schemes are recovered in 1D with a correction function defined as the Radau polynomials [28]. In particular, PyFR implemented the DG correction function.

The reader is referred to [4] for the construction of the FR schemes for the Navier-Stokes equations. Basically, an auxiliary variable $\mathbf{q}$ needs to be defined as the gradient of the conservative variables, and the second-order differential equations are rewritten as a first order system. Similar to the interface flux, a common solution is defined at each element interface, then a continuous solution is reconstructed from the discontinuous solution and $\mathbf{q}$ is computed with the continuous solution. The rest of the procedures are basically the same as those for the convection equations.

2.1.2 PyFR

The FR schemes, as well as the famous DG schemes and the SD schemes, are similar in the sense that they achieve higher orders by adding more solution points inside each element and approximating the solution with higher-order polynomials. By doing so, the solution is discontinuous at each element interface. Therefore this type of schemes can be called the discontinuous schemes. By nature the discontinuous schemes have strong element locality, i.e., they have small stencils, making them easily parallelizable and especially fit for the streaming architectures such as the Graphic Processing Unit (GPU).

PyFR is an open source Navier-Stokes solver based on the FR schemes and written in python [4]. It is designed to achieve high performance on a various of platforms, including the CPU and different types of GPU clusters, and is capable of handling mixed types of elements. PyFR has been chosen for this work for its adaptability and the fact that it has been well maintained. Some validation cases for PyFR can be found in their introduction paper [4].

2.2 The Plasma Actuator Model

The plasma actuator model Suzen *et al.* [1] proposed in 2007 was adopted for this study for its simplicity and its ability to correctly capture the qualitative behavior of the induced body force field and flow field. This model is based on the idea of solving the reduced Maxwell's equations and incorporating the effect of the plasma into the Navier-Stokes solver as a body force field, and is formally known as the electrostatic model.

Since the time scale of the plasma formulation is significantly smaller than the time

scale of the flow field, usually 1×10^{-8}s compared to 1×10^{-2}s, the problem can be decoupled into the body force formulation and the fluid flow response [26].

The supplied AC voltage on the electrodes normally has frequencies from 3 to 15 kHz, causing a time scale of 1×10^{-4}s for the plasma actuator operation. The alternation of the voltage applied on the electrodes is not resolved because of the several order of magnitude difference in the time scale of the AC and the flow field.

The body force can be expressed as

$$\vec{f_b} = \rho_c \vec{E}, \tag{2.12}$$

where $\vec{f_b}$ is the body force per unit volume, ρ_c is the charge density and $\vec{E}$ is the electric field.

It can be assumed that the plasma have significant amount of time to redistribute themselves so that the system is quasi-steady. In this case the Maxwell's equations give rise to $\nabla \times \vec{E} = 0$. Therefore a scaler potential can be defined:

$$\vec{E} = -\nabla\Phi, \tag{2.13}$$

where Φ is the electric potential. The reduced Maxwell's equations give

$$\nabla \cdot \left(\varepsilon \vec{E}\right) = \rho_c, \tag{2.14}$$

i.e.,

$$\nabla \cdot (\varepsilon \nabla\Phi) = -\rho_c, \tag{2.15}$$

where ε is the permittivity of the medium. The permittivity can be expressed as

$$\varepsilon = \varepsilon_r \varepsilon_0, \tag{2.16}$$

where ε_r is the relative permittivity and ε_0 is the permittivity of the free space.

The net charge density is defined as the difference between the positive charge of the ions and the negative charge of the electrons,

$$\rho_c = e\left(n_i - n_e\right), \tag{2.17}$$

where n_i and n_e are the number of particles in the plasma gas, and e is the charge of the electron. The Boltzmann relation of the particle density gives

$$n = n_0 \exp(\frac{e\Phi}{kT}), \tag{2.18}$$

where n_0 is the number of molecules that are ionized, k is the Boltzmann's constant, and T is the temperature of the plasma. Substitute Eq. (2.18) into Eq. (2.17) and use Taylor expansion, Eq. (2.17) can be written as:

$$\rho_c \approx -en_0 \left(\frac{e\Phi}{kT_i} + \frac{e\Phi}{kT_e}\right), \tag{2.19}$$

where T_i and T_e are the temperatures of the ion and the electron.

We introduce the Debye length λ_d as the characteristic length for electrostatic shielding in a plasma:

$$\lambda_d = \left[\frac{e^2 n_0}{\varepsilon_0}\left(\frac{e\Phi}{kT_i} + \frac{e\Phi}{kT_e}\right)\right]^{1/2}. \tag{2.20}$$

If we assume a value for it, the charge density can be found as

$$\rho_c/\varepsilon_0 = \left(-1/\lambda_d^2\right)\Phi. \tag{2.21}$$

Eq. (2.15) combined with Eq. (2.21) gives the Poisson equation for the electric potential

$$\nabla\cdot(\varepsilon_r\nabla\Phi) = \left(1/\lambda_d^2\right)\Phi. \tag{2.22}$$

Notice that inside the dielectric barrier the Debye length is taken as infinity.

Based on the fact that the gas is only weakly ionized, Suzen *et al.* proposed to decompose the electric potential into two parts in order to generate correct body force behavior. One part φ accounts for the external electric field, the other part ϕ accounts for the potential produced by the charge density:

$$\Phi = \varphi + \phi. \tag{2.23}$$

For weakly ionized gas the electric field caused by the electric charge can be ignored. With the assumption that the Debye length is small and the charge on the wall is not large, the distribution of charged species in the domain is governed by the potential caused by the charge on the wall and is largely unaffected by the external electric field. Therefore the equation for the external electric field and the charge density can be decoupled. For the potential associated with external electric field,

$$\nabla\cdot(\varepsilon\nabla\varphi) = 0, \tag{2.24}$$

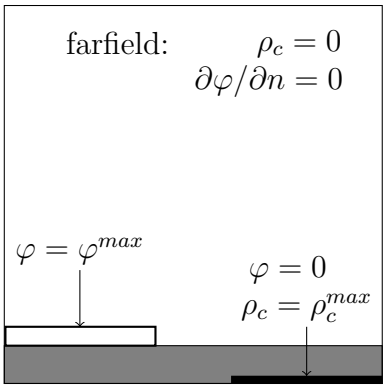

Figure 2.2: Boundary conditions for the plasma actuator model.

and for the charge density,

$$\nabla \cdot (\varepsilon \nabla \rho_c) = \rho_c / \lambda_d^2. \tag{2.25}$$

Eq. (2.24) and Eq. (2.25) can be solved separately. The boundary conditions imposed on the electrodes and the farfield are shown in Fig. 2.2. Notice that the charge density above the buried electrode needs to be empirically postulated.

A numerical experiment was carry out by Suzen *et al.* [1] with the model to find the ρ^{max} that induces a flow field with a maximum velocity that matches the experiment, approximately of magnitude $1\,\mathrm{m\,s^{-1}}$.

With the electric field and the charge density distribution computed, the body force can be calculated as

$$\vec{f_b} = -\rho_c \nabla \varphi. \tag{2.26}$$

Chapter 3

Computer Implementation

3.1 Solver for The Plasma Actuator Model: GetDP

The plasma actuator model described in chapter 2 involves solving two independent Poisson equations Eq. (2.24) and Eq. (2.25). The Poisson equations were solved with the open source unstructured differential equation solver GetDP [5]. GetDP acts as a general environment for solving differential equations. It requires the users to provide the mathematical formulation of the problem to be solved as GetDP objects, written in an input text data file.

The finite-element method was chosen as the spacial discretization scheme in GetDP and the Galerkin formulation was used. The body-force field was exported as a table with the coordinates and body-force values listed.

3.2 Implementation of The Flow Solver

PyFR was modified to add the body-force as a source term for the momentum equations. Several small modifications were made to PyFR:

- A table reader was added for reading in the body-force files;
- Two methods were added to the *system* class where the system data is stored to interpolate the body force from the plasma model grid to the flow field solution points according to the order of the scheme used;
- A pointwise computation kernel was modified to add the source terms to the computed divergence of the flux.

The solver was run on a 16-core CPU with openmp.

Chapter 4

Results and Discussion

4.1 Results of The plasma Actuator Model

The mesh used in this problem was generated in Gmsh [6] with the Delaunay method. It contains 164645 nodes and 336360 elements to give a proper resolution.

The geometric parameters and the boundary conditions for the model basically followed the paper Suzen etc. published in 2007 [1], except that the plasma actuators are mounted on a circular cylinder. The cylinder has a diameter of 100 mm. Both of the electrodes are of length 10 mm and thickness 0.102 mm. The streamwise spacing was set to be 1 mm to eliminate abnormal body force magnitude concentration on the edge on the exposed electrode. The downstream direction is the direction from the exposed electrode towards the embedded electrode in the flow field simulations.

The plasma actuators are located at ± 90 deg with respect to the incoming flow direction. These locations were chosen in order for the actuators to be close to the flow separation point.

The computed distributions of the electric potential and the charge density in Fig. 4.1 and Fig. 4.2 agree with the results from Suzen etc.. The induced body force magnitude distribution also agrees with their result. A zoomed-in view of the body force field around the upper actuator is given in Fig. 4.3.

The charge density has a large concentration on the embedded electrode, resulting in an area with large body force generally pointing downward above the embedded electrode. Later in this chapter, it will be shown that this typical body force field causes a jet towards the downstream direction.

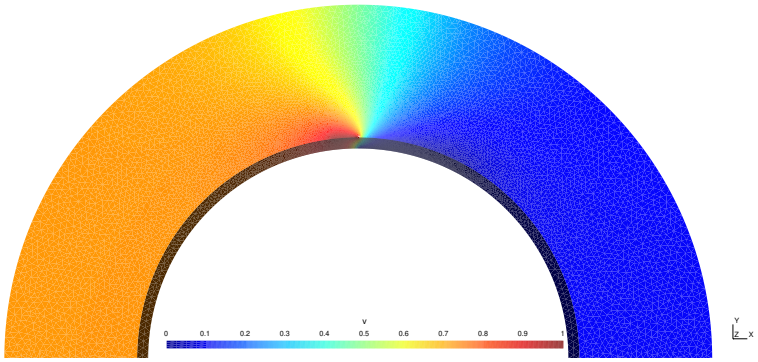

Figure 4.1: Electric potential distribution.

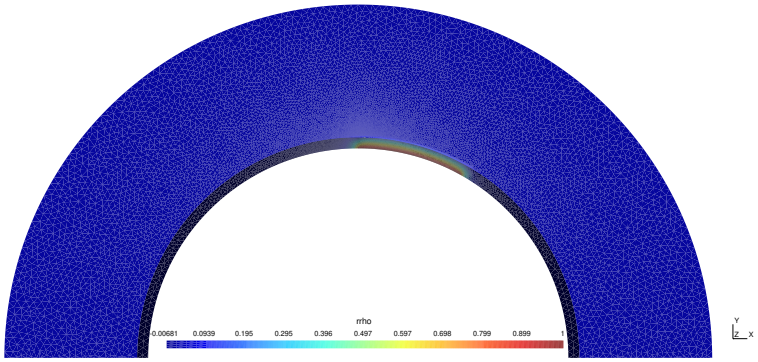

Figure 4.2: Charge density distribution.

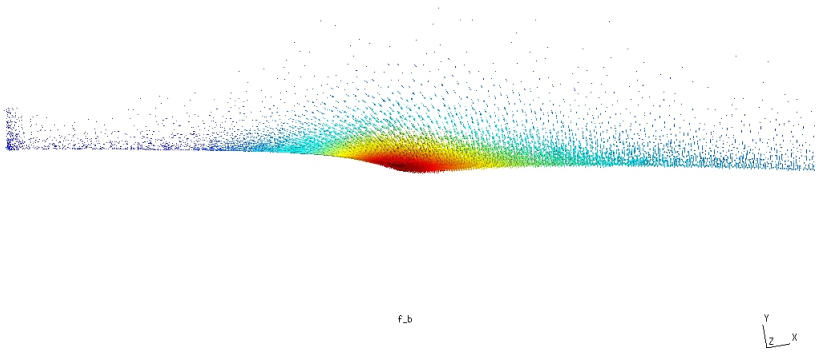

Figure 4.3: Zoomed-in view of the body force field above the embedded electrode.

4.2 Flow Control Results

The grid used for the flow field computation credits to PyFR's development team. The grid contains 7345 nodes and 3526 elements, including 196 9-node rectangles and 3221 6-node triangles. The mesh is shown in Fig. 4.4. Geometric high-order elements, usually referred to as curved elements are necessary on curved boundaries for high order schemes to keep high order convergence rates [35].

4.2.1 Plasma Induced Flow Field

The body force field was added into a stationary flow field to produce the plasma actuator induced flow. A fifth-order scheme was used in this case. The maximum electric potential ϕ^{max} and the maximum charge density were set to be $5 \times 10^5\,\mathrm{V}$

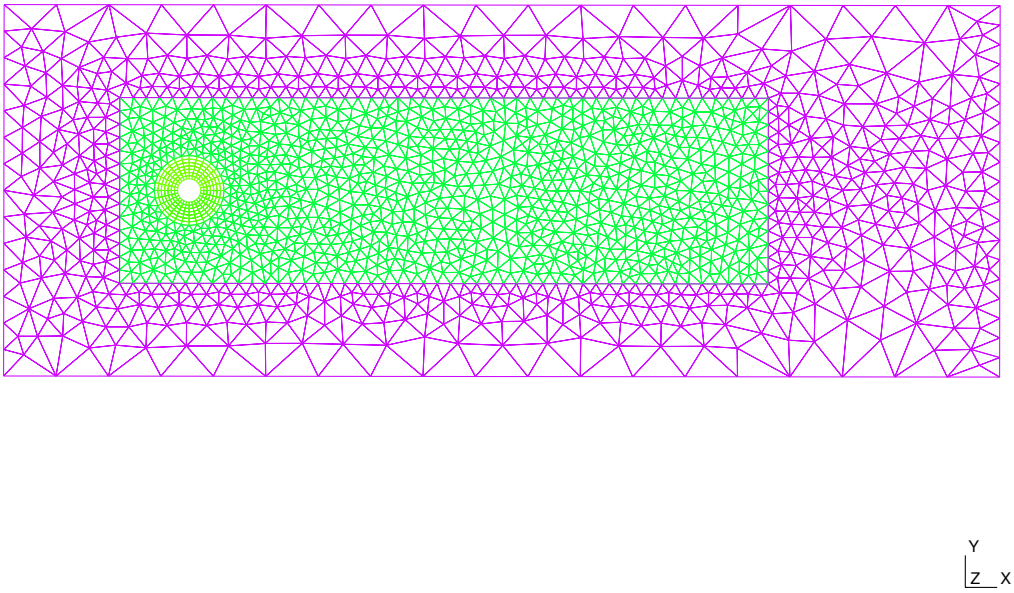

Figure 4.4: Grid used for flow field computation.

and $7.5\,\mathrm{C\,m^{-2}}$ respectively. The voltage applied in this computation is higher than the normal voltage applied to the plasma actuators in order to create an induced flow field with a reasonably large Mach number for the compressible flow solver, since Mach numbers one magnitude lower would cause a prohibitively low convergence rate. Although the velocity used in our case is larger than most flow control experiments done on plasma actuator, since the inlet Mach number is still on the magnitude of 0.1, the computations are still restricted in the incompressible range. With a sufficiently low incoming Mach number, the compressibility generally does not have an effect on the flow around a cylinder. By matching the Reynolds number in the computations and the comparison experiments, the results are still valid for a qualitative study.

It can be seen clearly from the results that the actuator initially induces a counterclockwise spanwise vortex, which is the observation in many experiments [3] as well as computational results [26]. The induced vortex moves following a trajectory studied in the paper by Whalley and Choi [3]. The nondimensional time t^* is defined as $t^* = tU_0^2/\nu$, where U_0 is the maximum induced velocity and ν is the kinematic viscosity of the air. Same as what is observed in the experiments of Whalley etc., the computation results suggest that the maximum induced velocity becomes constant after it reaches certain value. The spatial coordinates are also nondimensionalized with U_0 and ν as $x^* = xU_0/\nu$ and $y^* = yU_0/\nu$.

The velocity vector field at $t^* = 13185$ and $t^* = 26370$ are shown in Fig. 4.5. The nondimensional velocity $u^* = u/U_0$. Nondimensional time and coordinates are used to keep consistent with the study of Whalley etc.. Although due to the limitation of spacial resolution of the grid, the positions of the center of the vortex can not be found precisely. It can be seen from the figures that the induced vortex follows approximately the same trajectory as in the experimental results. Whalley etc. have also found that the vortex is self-similar at different time steps, which is also the case

in this computation study.

An explanation of the formulation and movement of the plasma induced vortex is given in the paper of Whalley etc.. The momentum applied on the fluid in the vicinity of the plasma drives the fluid to form a jet. To replenish the fluid that has been ejected, entrainment happens for the fluid above the embedded electrode thus forms the vortex. Along with the initial vortex secondary vorticity is generated to keep the no-slip condition on the wall. They wrap around the initial vortex and push it forward. A schematic of this explanation is given in Fig. 4.7.

As the vortex moves towards the back of the cylinder, a jet originating from the edge of the exposed electrode can be clearly observed. The jet adheres to the surface of the cylinder under Coanda effect, which is believed to be the reason of the delayed flow separation in the cases of bluff body flow control [2]. As the flow field develops, secondary vortices are generated and the flow field becomes more complex. Vortices from the opposite sides of the cylinder meet at the rear stagnation point, as shown in Fig. 4.6.

4.2.2 Order of Accuracy Study of The Flow Solver

A two-dimensional flow around a cylinder was first run with PyFR as a reference case with a Reynolds number 6.6×10^3 and Mach number 0.338. The solver was run with both the third-order and the fifth-order options to give a comparison of different orders of accuracy.

In order to find the Karman vortex shedding frequency, the pressure was sampled at $x/D = 2$,$y = 0$ for over 80 convective time with a nondimensional frequency 2.5. A discrete Fourier transform was performed. The pressure fluctuation and its Fourier

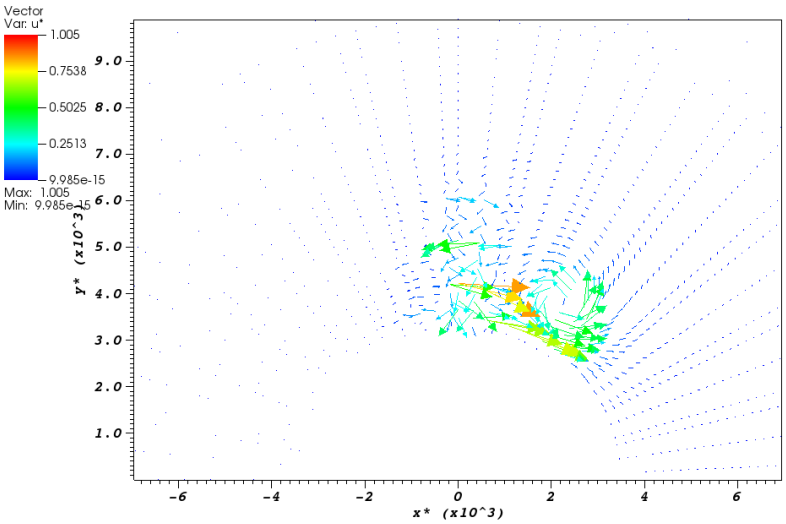

(a) $t^* = 13185$

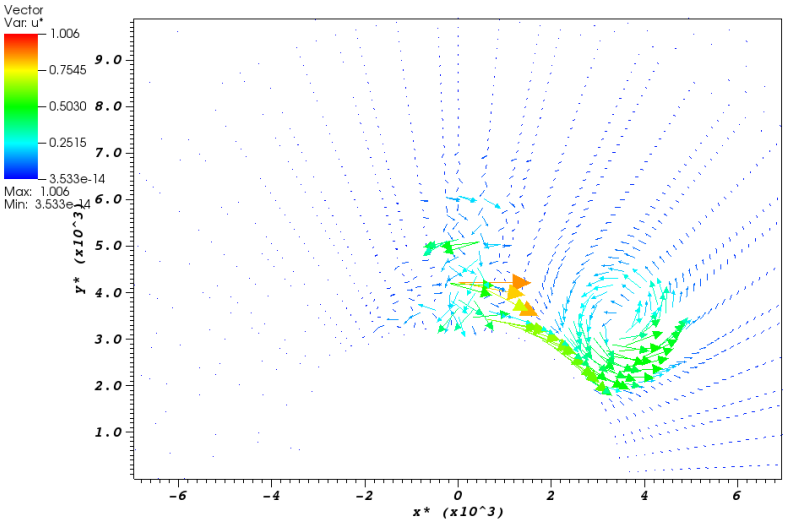

(b) $t^* = 26370$

Figure 4.5: The plasma induced vortex.

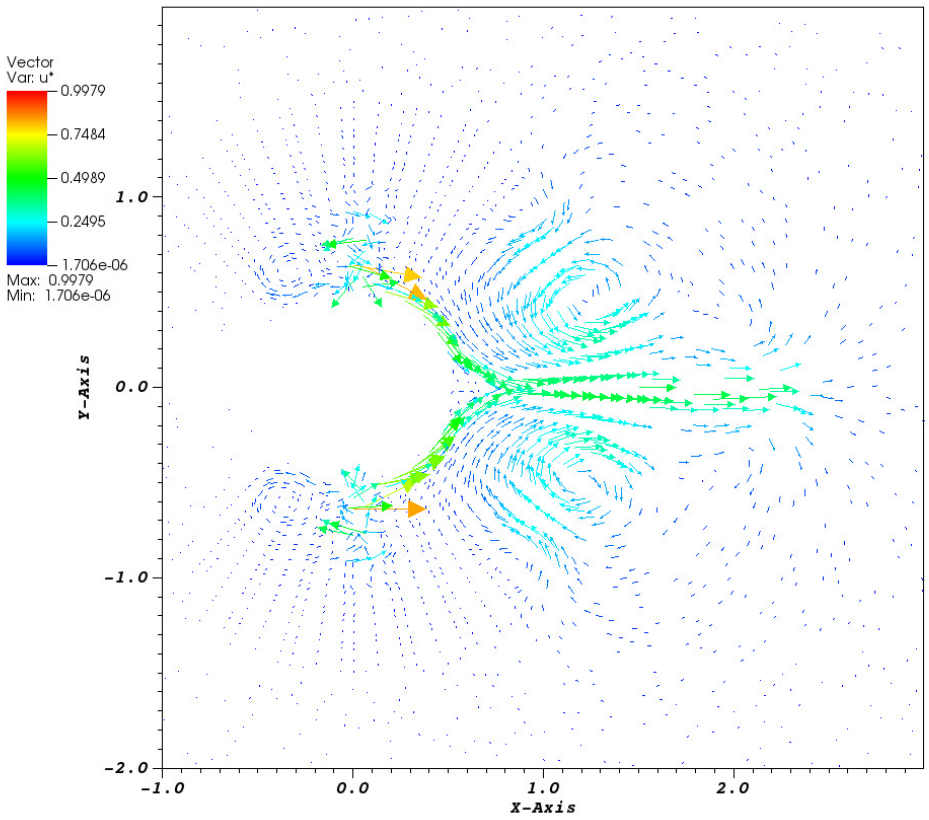

Figure 4.6: Developed plasma induced vorticity.

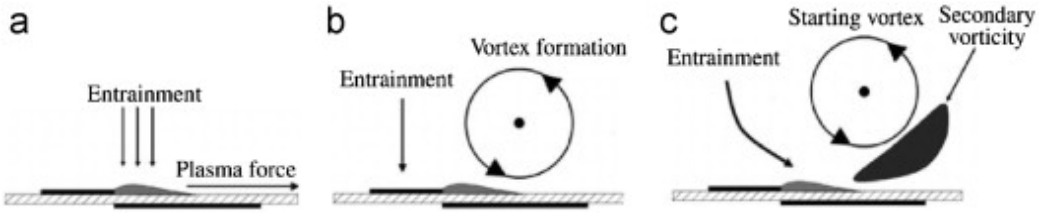

Figure 4.7: Schematic of the mechanism of the induced vortex [3].

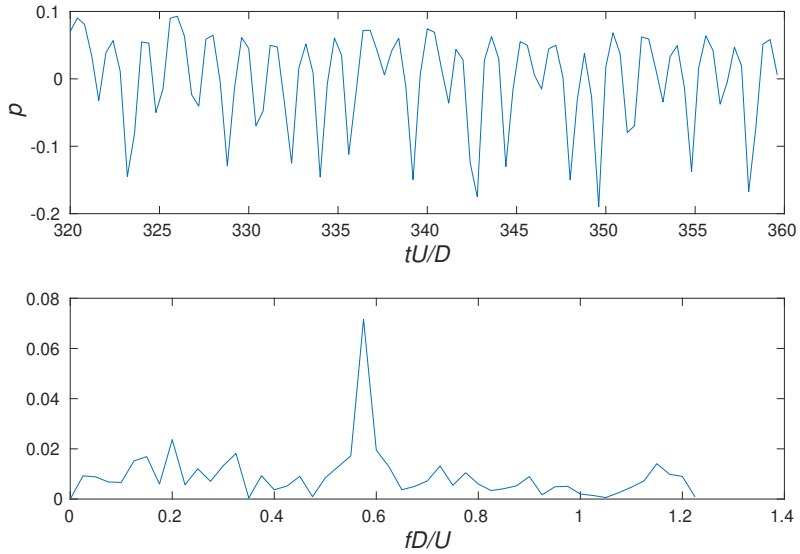

Figure 4.8: Fourier transform of the pressure fluctuation at $x/D = 2, y = 0$ (p=5).

transform for the fifth-order case are shown in Fig. 4.8. Notice that the wake is influenced by vortex shedding from both sides of the cylinder, therefore the detected frequency is twice the vortex shedding frequency. Non-dimensional unsteady vortex shedding frequency of 0.388 and 0.288 was found in the third-order and fifth-order cases, respectively. Both cases show a shedding frequency larger than the reported value 0.21 in the experiments [20]. This could be caused by the lack of spacial resolution, or the limitation of 2D computations. In a 2D computation of flow around a circular cylinder, an overprediction of the shedding frequency was found [36]. Due to the limitation of computation resources, the specific causation of the overpredicted shedding frequency was not studied in this thesis and is proposed as future work.

A comparison of the vorticity field for the third-order and the fifth-order cases is given in Fig. 4.10. The nondimensional vorticity ω^* is defined as $\omega^* = \omega L/U$. The wake behind the cylinder for the 3rd-order case appears to be smaller, and the separation happens further downstream. The strength of the first downstream vortex is probed for both cases. The 3rd-order case shows weaker vortex strength, which suggests

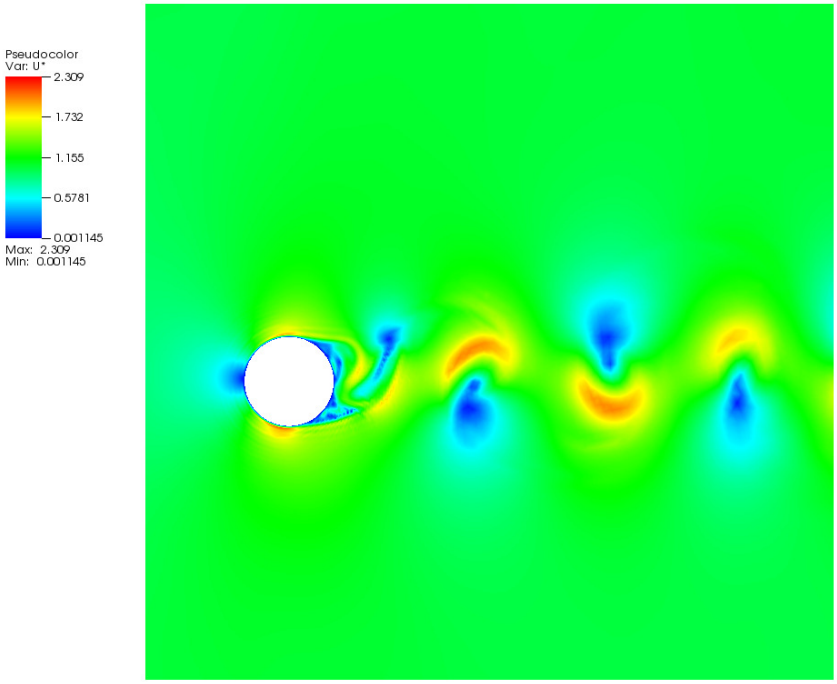

(a) Velocity magnitude distribution.

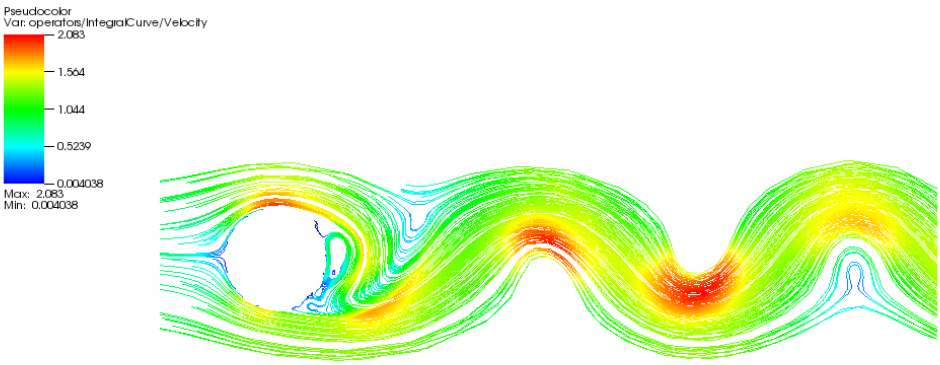

(b) Streamlines.

Figure 4.9: Flow field without the plasma actuators (5th-order).

a larger artificial dissipation. The time-averaged pressure drag coefficients for both cases are calculated. The 5th-order case gives a drag coefficient of 1.4437, which is slightly larger than what has been reported in the experiments [37]. A drag larger than the experimental value was also presented in a large eddy simulation of flow around a circular cylinder[24]. However the 3rd-order case produces a much smaller value of 0.6941. This could be foreseen from the fact that the wake behind the 3rd-order case is much smaller.

The comparisons above suggest that the 3rd-order scheme does not provide enough resolution in this case. Therefore the 5th-order case was chosen as the base case, and the computations with plasma on were run with the 5th-order scheme. The normalized velocity magnitude distribution and the streamlines of the fifth-order case are shown in Fig. 4.9.

4.2.3 Flow Around a Cylinder with Plasma Flow Control

A body force field with the same magnitude as in section 2 was added into the flow field. The altered velocity magnitude distribution and streamlines are shown in Fig. 4.11. The vorticity fields at 3 time instances during one vortex shedding period are shown in Fig. 4.12. It can be seen clearly from the figures that there is a smaller wake behind the cylinder compared to the simulation without the plasma actuators. Although the vortex shedding is not completely eliminated, the strength of the vortices is reduced.

Fig. 4.13 shows a comparison of the time-averaged velocity profile at $x/D = 3$ for the cases with and without the actuators. The figure indicates that with the plasma actuators both the size of the wake and the velocity defect in the wake are reduced. Both cases were run for more than 500 convective time units before taking the time-

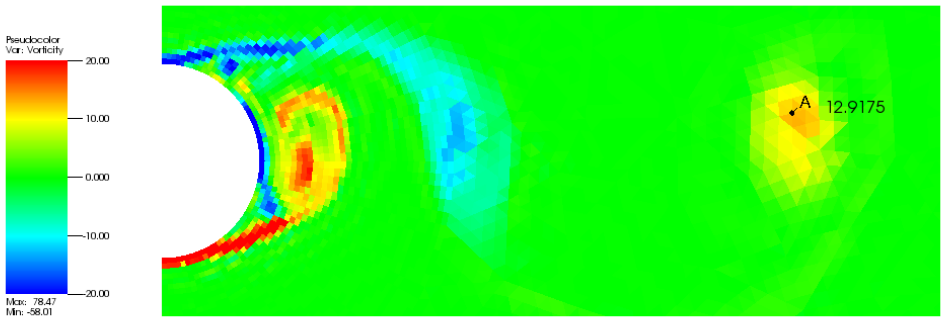

(a)

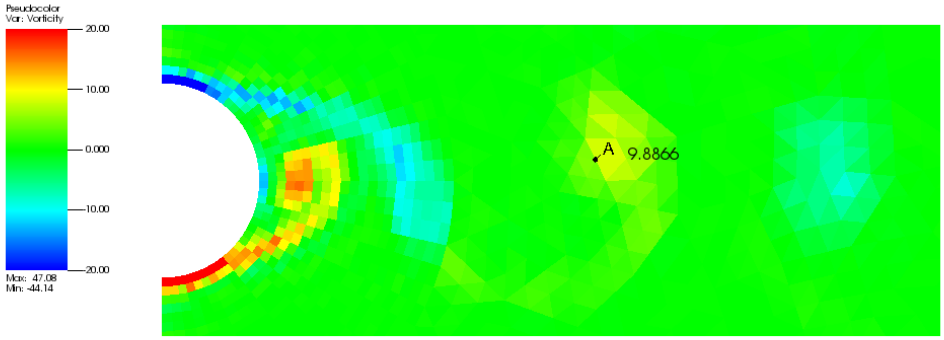

(b)

Figure 4.10: Comparison of near wake vortex strength. (a) results by the 5th-order scheme; (b) results by the 3rd-order cases.

Table 4.1: Time-averaged drag coefficients.

	Base case	90 deg	100 deg
C_D	1.4437	0.2584	0.1639

average, and the time-average was taken over 20 cycles of the Karman vortex shedding. Similar results can be found in an experimental study done in 2008 by Thomas etc. [2].

The pressure coefficient on the cylinder surface is shown in Fig. 4.14. Notice that a pair of local extreme with large pressure is presented at approximately the actuator locations in the case with the actuators. This is an indication of the local alternation of the flow caused by the actuators. The local large pressure could be caused by the entrainment of the air, which creates a stagnation point on the cylinder surface close to the actuators.

The fluctuation of the lift and drag acting on the cylinder is presented in Fig. 4.15, where t^* is the convective time. The amplitudes of both the lift and drag fluctuation are largely reduced with the effect of the actuators. The case with the actuators shows a slightly larger vortex shedding frequency, which is also observed in a simulation of steady actuation [23]. This could be related to the shrink of the width of the wake.

The time-averaged drag of the cases with and without the actuators are listed in Table 4.1. A drag reduction of 82.1% is shown. In an experiment done by Thomas. etc with plasma actuators mounted on a circular cylinder, a drag reduction of 90% was reported [2].

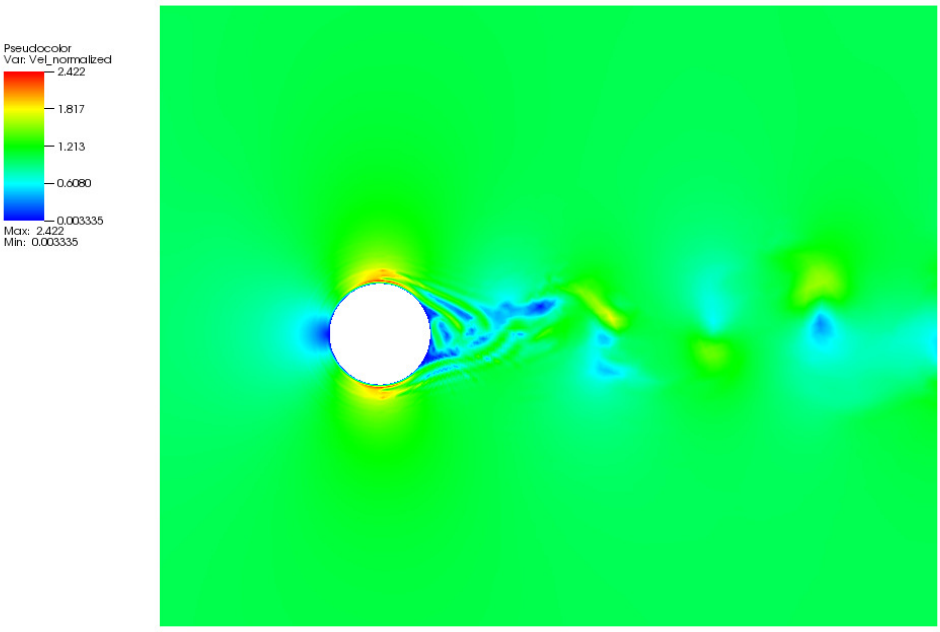

(a) Velocity magnitude distribution.

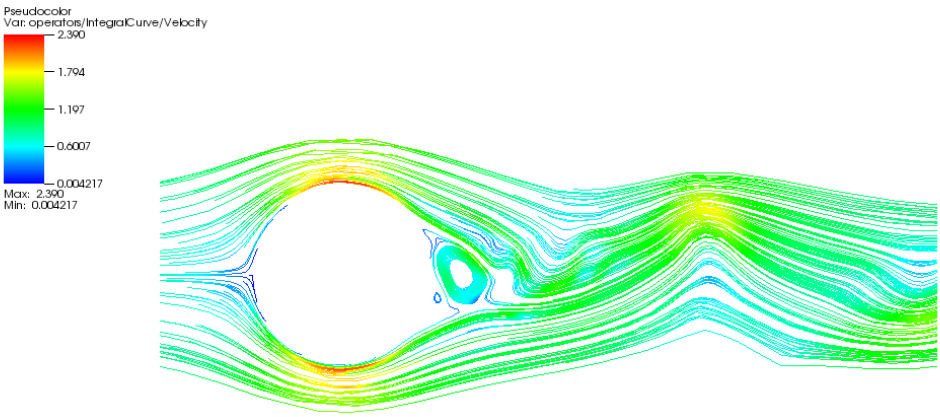

(b) Streamlines.

Figure 4.11: Flow field with actuators mounted at ±90 deg.

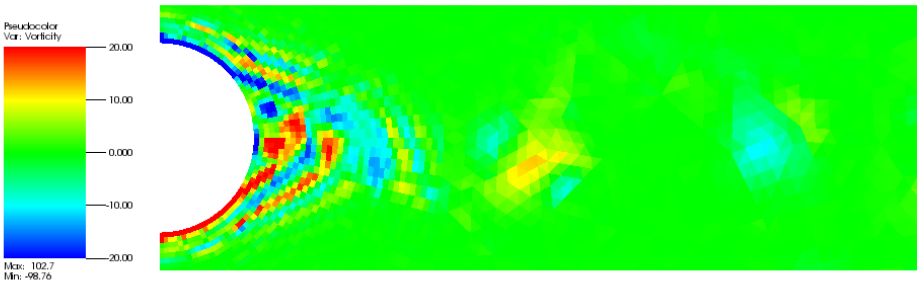

(a) $t/T = 0.0$

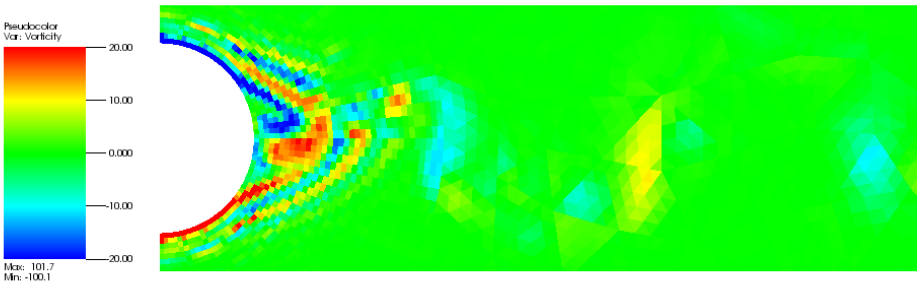

(b) $t/T = 0.25$

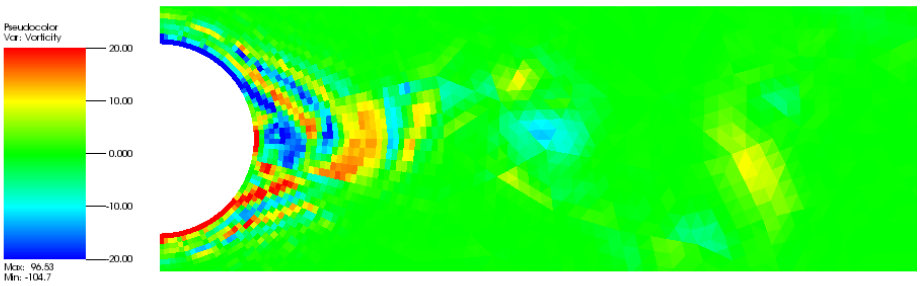

(c) $t/T = 0.50$

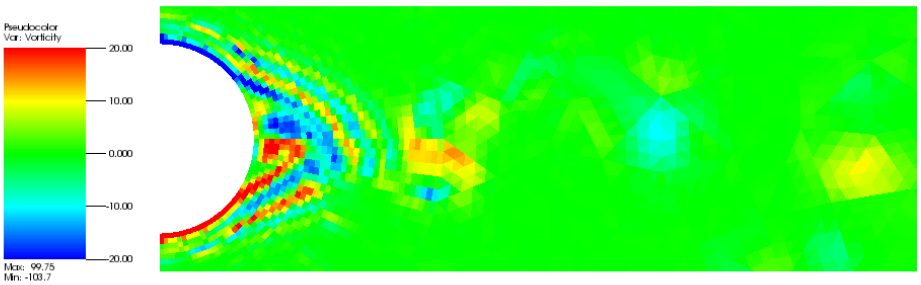

(d) $t/T = 0.75$

Figure 4.12: Vorticity field with actuators mounted at ±90 deg.

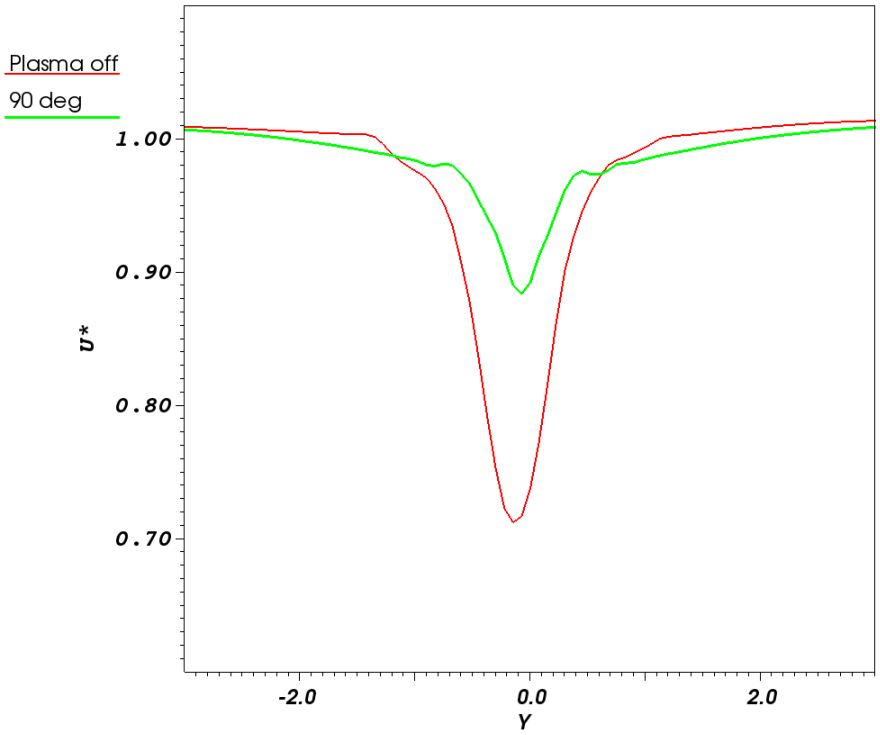

Figure 4.13: Wake velocity profile at $x/D = 3$.

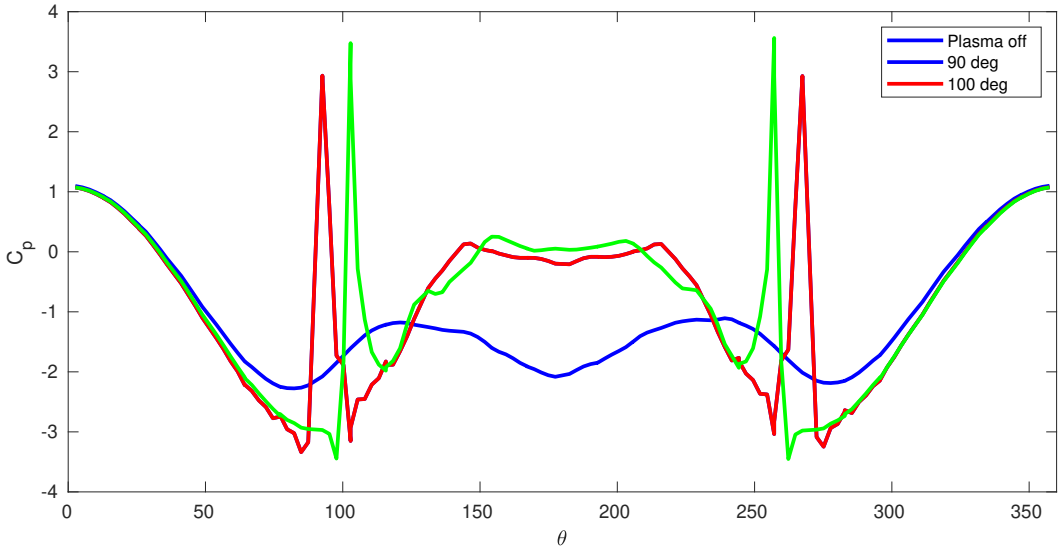

Figure 4.14: Pressure distribution on the cylinder surface.

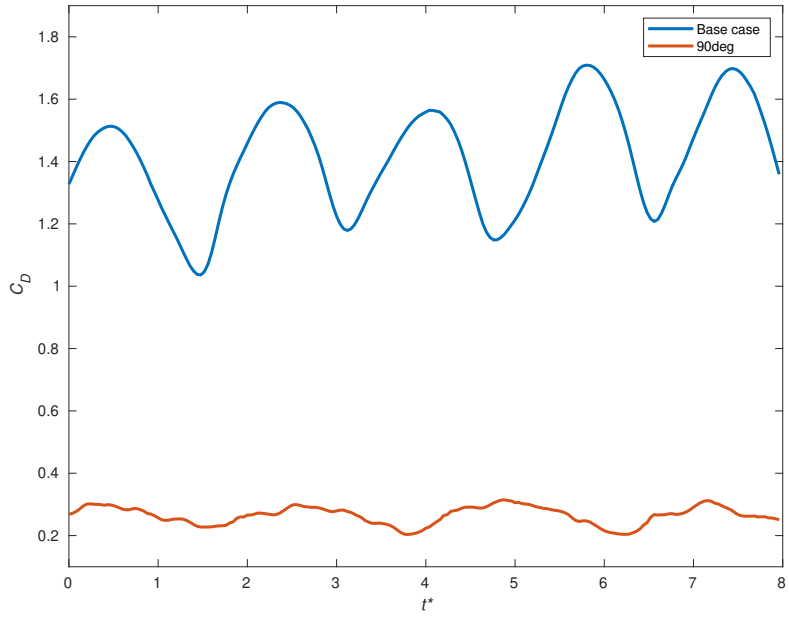

(a) Drag fluctuation.

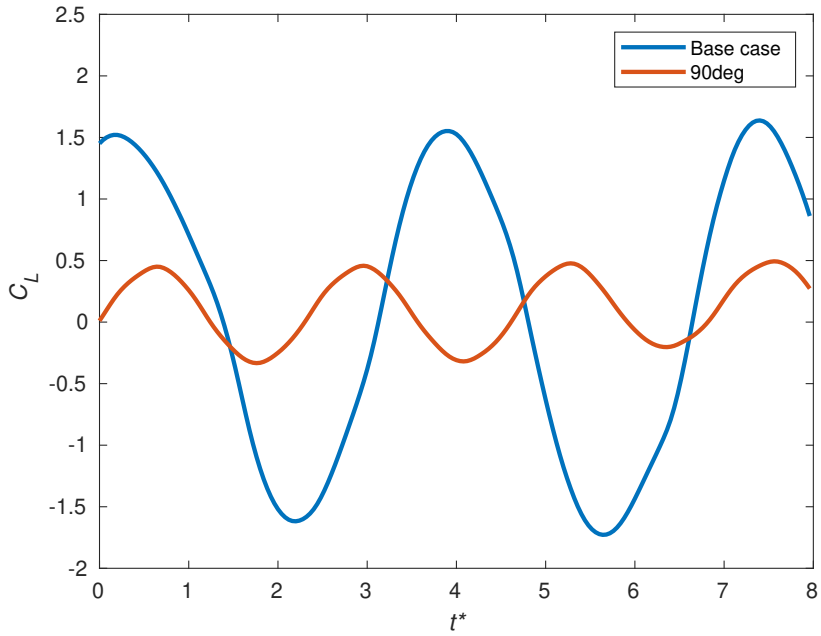

(b) Lift fluctuation.

Figure 4.15: Fluctuation of drag and lift acting on the cylinder.

4.2.4 Parametric Study of the Actuator Locations

The locations of the plasma actuators on the cylinder surface were changed from ±90 deg to ±100 deg, closer to the separation point, to study the effect of the locations. The strength of the actuation was lowered to 80% to keep the local extreme Mach number lower than 1.

The velocity magnitude distribution and streamlines are shown in Fig. 4.16. A strongly-suppressed vortex shedding is shown, and the wake becomes smaller that the case with actuators at ±90 deg. The pressure distribution on the cylinder surface is shown in Fig. 4.14. The pressure distribution indicate as a slightly smaller wake with the actuators mounted at ±100 deg compared withe the ±90 case.

The drag coefficient of the cases with the actuators placed at ±90 deg and ±90 deg are listed in Table 4.1. The case with the actuators at ±100 deg produces a drag that is nearly 40% lower than the ±90 deg case.

The results of the parametric study indicate that the effectiveness of the plasma actuation is sensitive to the location of the actuators. A location that is close to the separation point can largely improve the performance of the actuator.

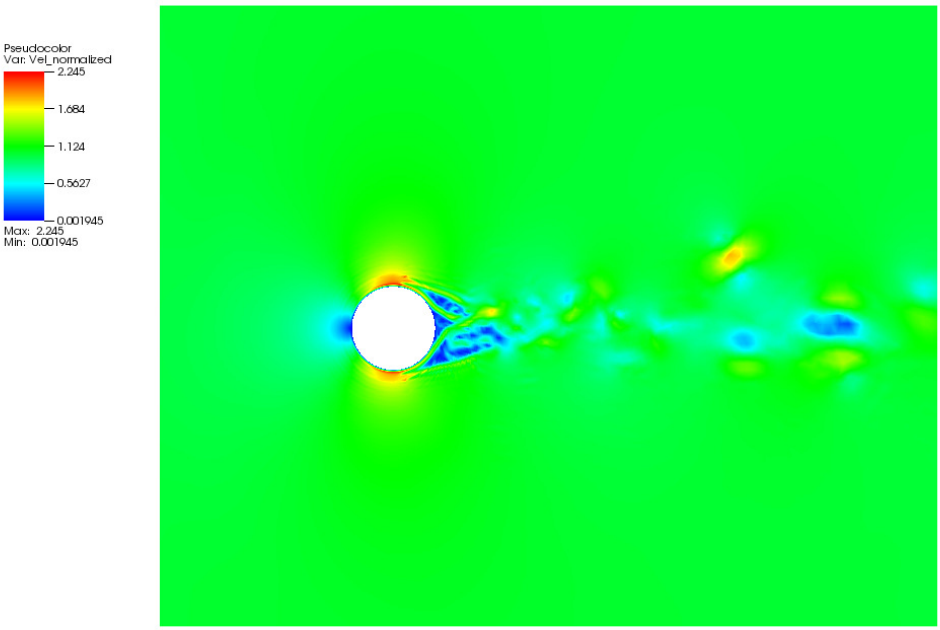

(a) Velocity magnitude distribution.

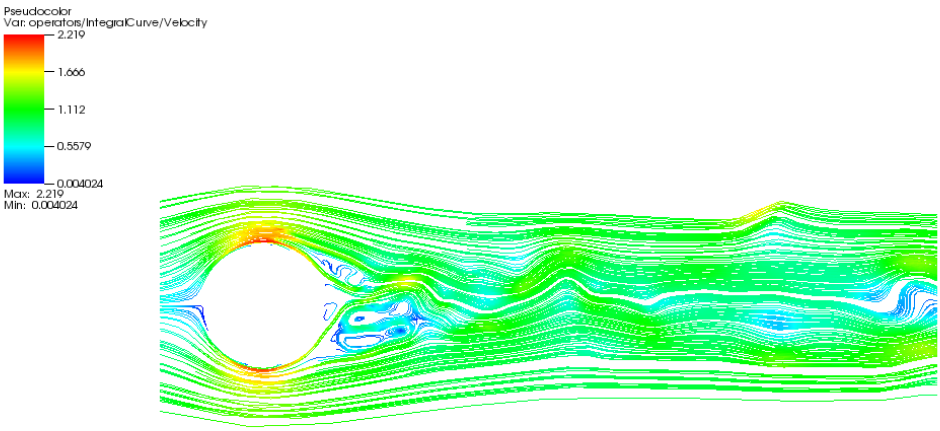

(b) Streamlines.

Figure 4.16: Flow field with actuators mounted at ±100 deg.

Chapter 5

Conclusion

The results in this thesis demonstrated the feasibility to design the parameters of the plasma actuator implementations to improve their performance via computations. The results of the parametric study indicates the sensitivity of the actuator performance to their locations. The optimal location of the actuators can be studied with a particular shape of the bluff body to provide specific suggestions on the placement of the actuators.

An improvement that could be made in the future is to use a more sophisticated model. The currently model has the problem of producing an incorrect body force magnitude scaling with the AC voltage applied. The charge density on the embedded electrode has to be arbitrarily postulated, making it less precise. Furthermore, an improved model could possibly capture the spacial distribution of the body force more accurately.

The computations in this study were restricted to 2D due to the limitation of time. It should be mentioned that the extension to a 3D case does not add any technical difficulty in this case. However running large scale 3D cases with high-order schemes

has a high requirement on the computer hardware and would take a fairly long computation time. A demonstration of the computational effort required for a 3D case of flow around a cylinder with PyFR can be found in reference [38]. With our current 16-core CPU, the computation time needed for a 3D case is prohibitive.

The advantages of using high-order schemes will be demonstrated more clearly with the presence of turbulence when running 3D cases. With the work done to improve the performance of PyFR on various hardware platforms, it is a favorable resource to run cases that require high resolutions.

Many other factors are commonly considered effective, possible future work includes:

- The frequency and the duty cycle when using unsteady actuation;
- The number of pairs of actuators used;
- The spanwise arrangement of the actuators.

The effectiveness of the actuation has been proven to be particularly sensitive to the unsteady actuation frequency [2]. The study of unsteady actuation requires to make the body force field added into the flow solver time-dependent, and is proposed as future work.

The work in this thesis made it possible to incorporate the influence of plasma actuators into the flow solver, therefore provided a starting point for future implementations of PyFR to plasma flow control studies.

Bibliography

[1] Yildirim Suzen, George Huang, and David Ashpis. Numerical simulations of flow separation control in low-pressure turbines using plasma actuators. In *45th AIAA Aerospace Sciences Meeting and Exhibit*, page 937, 2007.

[2] Flint O Thomas, Alexey Kozlov, and Thomas C Corke. Plasma actuators for cylinder flow control and noise reduction. *AIAA journal*, 46(8):1921–1931, 2008.

[3] Richard D Whalley and Kwing-So Choi. The starting vortex in quiescent air induced by dielectric-barrier-discharge plasma. *Journal of Fluid Mechanics*, 703:192–203, 2012.

[4] F.D. Witherden, A.M. Farrington, and P.E. Vincent. Pyfr: An open source framework for solving advectiondiffusion type problems on streaming architectures using the flux reconstruction approach. *Computer Physics Communications*, 185(11):3028 – 3040, 2014.

[5] P. Dular and C. Geuzaine. GetDP reference manual: the documentation for GetDP, a general environment for the treatment of discrete problems. `http://getdp.info`.

[6] Christophe Geuzaine and Jean-François Remacle. Gmsh: A 3-d finite element mesh generator with built-in pre-and post-processing facilities. *International journal for numerical methods in engineering*, 79(11):1309–1331, 2009.

[7] Hank Childs, Eric Brugger, Brad Whitlock, Jeremy Meredith, Sean Ahern, David Pugmire, Kathleen Biagas, Mark Miller, Cyrus Harrison, Gunther H. Weber, Hari Krishnan, Thomas Fogal, Allen Sanderson, Christoph Garth, E. Wes Bethel, David Camp, Oliver Rübel, Marc Durant, Jean M. Favre, and Paul Navrátil. VisIt: An End-User Tool For Visualizing and Analyzing Very Large Data. In *High Performance Visualization–Enabling Extreme-Scale Scientific Insight*, pages 357–372. Oct 2012.

[8] Thomas C Corke, C Lon Enloe, and Stephen P Wilkinson. Dielectric barrier discharge plasma actuators for flow control. *Annual review of fluid mechanics*, 42:505–529, 2010.

[9] JP Boeuf, Y Lagmich, Th Unfer, Th Callegari, and LC Pitchford. Electrohydrodynamic force in dielectric barrier discharge plasma actuators. *Journal of Physics D: Applied Physics*, 40(3):652, 2007.

[10] Feng Liu, Shijun Luo, Chao Gao, Xuanshi Meng, Jiangnan Hao, Jianlei Wang, and Zijie Zhao. Flow control over a conical forebody using duty-cycled plasma actuators. *AIAA journal*, 46(11):2969–2973, 2008.

[11] Jianlei Wang, Huaxing Li, Feng Liu, and Shijun Luo. Characteristics of forebody separate flow at high angle of attack under plasma control. *Modern Physics Letters B*, 24(13):1401–1404, 2010.

[12] Zijie Zhao, Chao Gao, Feng Liu, and Shijun Luo. Plasma flow control over forebody at high angles of attack. *Modern Physics Letters B*, 24(13):1405–1408, 2010.

[13] Yuexiao Long, Huaxing Li, Xuanshi Meng, Feng Liu, and Shijun Luo. Influence of actuating position on asymmetric vortex control with nanosecond pulse dbd plasma actuators. *IEEE Transactions on Plasma Science*, 44(11):2785–2795, 2016.

[14] Xuanshi Meng, Yuexiao Long, Jianlei Wang, Feng Liu, and Shijun Luo. Dynamics and control of the vortex flow behind a slender conical forebody by a pair of plasma actuators. *Physics of Fluids*, 30(2):024101, 2018.

[15] Thomas McLaughlin, Matthew Munska, Joseph Vaeth, Travis Dauwalter, Jeffrey Goode, and Stefan Siegel. Plasma-based actuators for cylinder wake vortex control. In *2nd AIAA Flow Control Conference*, page 2129, 2004.

[16] Martiqua L Post and Thomas C Corke. Separation control on high angle of attack airfoil using plasma actuators. *AIAA journal*, 42(11):2177–2184, 2004.

[17] Junhui Huang, Thomas Corke, and Flint Thomas. Separation control over low pressure turbine blades. In *APS Division of Fluid Dynamics Meeting Abstracts*, 2003.

[18] Timothy Jukes, Kwing-So Choi, Graham Johnson, and Simon Scott. Turbulent drag reduction by surface plasma through spanwise flow oscillation. In *3rd AIAA Flow Control Conference*, page 3693, 2006.

[19] Xuanshi Meng, Haiyang Hu, Xu Yan, Feng Liu, and Shijun Luo. Lift improvements using duty-cycled plasma actuation at low reynolds numbers. *Aerospace Science and Technology*, 72:123–133, 2018.

[20] Charles HK Williamson. Vortex dynamics in the cylinder wake. *Annual review of fluid mechanics*, 28(1):477–539, 1996.

[21] Y Sung, W Kim, MG Mungal, and MA Cappelli. Aerodynamic modification of flow over bluff objects by plasma actuation. *Experiments in Fluids*, 41(3):479–486, 2006.

[22] Benjamin Mertz and Thomas Corke. Time-dependent dielectric barrier discharge plasma actuator modeling. In *47th AIAA Aerospace Sciences Meeting including The New Horizons Forum and Aerospace Exposition*, page 1083, 2009.

[23] Donald P Rizzetta and Miguel R Visbal. Large eddy simulation of plasma-based control strategies for bluff body flow. *AIAA journal*, 47(3):717–729, 2009.

[24] Dongjoo Kim and Meng Wang. Large-eddy simulation of flow over a circular cylinder with plasma-based control. In *47th AIAA Aerospace Sciences Meeting including The New Horizons Forum and Aerospace Exposition*, page 1080, 2009.

[25] Timothy Jukes and K-S Choi. Active control of a cylinder wake using surface plasma. In *IUTAM Symposium on Unsteady Separated Flows and their Control*, pages 539–550. Springer, 2009.

[26] Dmitriy M Orlov. *Modelling and simulation of single dielectric barrier discharge plasma actuators*. 2006.

[27] JP Boeuf and LC Pitchford. Electrohydrodynamic force and aerodynamic flow acceleration in surface dielectric barrier discharge. *Journal of Applied Physics*, 97(10):103307, 2005.

[28] Ht T Huynh. A flux reconstruction approach to high-order schemes including discontinuous galerkin methods. In *18th AIAA Computational Fluid Dynamics Conference*, page 4079, 2007.

[29] Peter E Vincent, Patrice Castonguay, and Antony Jameson. A new class of high-order energy stable flux reconstruction schemes. *Journal of Scientific Computing*, 47(1):50–72, 2011.

[30] Hung T Huynh. A reconstruction approach to high-order schemnes including discontinuous galerkin for diffusion. In *47th AIAA Aerospace Sciences Meeting Including the New Horizons Forum and Aerospace Exposition*, page 403, 2009.

[31] P Castonguay, DM Williams, PE Vincent, and A Jameson. Energy stable flux reconstruction schemes for advection–diffusion problems. *Computer Methods in Applied Mechanics and Engineering*, 267:400–417, 2013.

[32] Patrice Castonguay, Peter E Vincent, and Antony Jameson. A new class of high-order energy stable flux reconstruction schemes for triangular elements. *Journal of Scientific Computing*, 51(1):224–256, 2012.

[33] Patrice Castonguay. *High-order energy stable flux reconstruction schemes for fluid flow simulations on unstructured grids*. PhD thesis, Citeseer, 2012.

[34] Philip L Roe. Approximate riemann solvers, parameter vectors, and difference schemes. *Journal of computational physics*, 43(2):357–372, 1981.

[35] Krzysztof J Fidkowski, Todd A Oliver, James Lu, and David L Darmofal. p-multigrid solution of high-order discontinuous galerkin discretizations of the compressible navier–stokes equations. *Journal of Computational Physics*, 207(1):92–113, 2005.

[36] Mani Sadeghi. *Computation of mistuning effects on blade flutter in a cascade*. PhD thesis, University of California, Irvine, 2001.

[37] Bengt Fornberg. A numerical study of steady viscous flow past a circular cylinder. *Journal of Fluid Mechanics*, 98(4):819–855, 1980.

[38] Freddie D Witherden, Brian C Vermeire, and Peter E Vincent. Heterogeneous computing on mixed unstructured grids with pyfr. *Computers & Fluids*, 120:173–186, 2015.